Earth, Planets and Space

FULL PAPER Open Access

Resonant interaction of relativistic electrons with realistic electromagnetic ion–cyclotron wave packets

Veronika S. Grach[1*], Andrei G. Demekhov[1,2] and Alexey V. Larchenko[2]

Abstract

We study the influence of real structure of electromagnetic ion-cyclotron wave packets in the Earth's radiation belts on precipitation of relativistic electrons. Automatic algorithm is used to distinguish isolated elements (wave packets) and obtain their amplitude and frequency profiles from satellite observations by Van Allen Probe B. We focus on rising-tone EMIC wave packets in the proton band, with a maximum amplitude of 1.2–1.6 nT. The resonant interaction of the considered wave packets with relativistic electrons 1.5–9 MeV is studied by numerical simulations. The precipitating fluxes are formed as a result of both linear and nonlinear interaction; for energies 2–5 MeV precipitating fluxes are close to the strong diffusion limit. The evolution of precipitating fluxes is influenced by generation of higher-frequency waves at the packet trailing edge near the equator and dissipation of lower-frequency waves in the He^+ cyclotron resonance region at the leading edge. The wave packet amplitude modulation leads to a significant change of precipitated particles energy spectrum during short intervals of less than 1 minute. For short time intervals about 10–15 s, the approximation of each local amplitude maximum of the wave packet by a Gaussian amplitude profile and a linear frequency drift gives a satisfactory description of the resonant interaction.

Keywords: Resonant interaction, Radiation belts, Precipitation, Relativistic electrons, EMIC waves

Introduction

The dynamics of Earth radiation belts has been studied experimentally and theoretically for many years (Kennel and Petschek 1966; Tverskoy 1969; Lyons and Thorne 1973; Bespalov and Trakhtengerts 1986; Trakhtengerts and Rycroft 2000; Millan and Thorne 2007; Morley et al. 2010; Li and Hudson 2019). Among various phenomena of radiation belt physics, an important place is occupied by precipitation of relativistic electrons. The precipitating fluxes of relativistic electrons play an important role in depletion of radiation belts that pose a danger for the operation of geosynchronous satellites; precipitating relativistic electrons can also significantly affect atmospheric chemistry (Krivolutsky and Repnev 2012; Mironova et al. 2015).

One of the possible mechanisms of relativistic electron precipitation is their resonant interaction with electromagnetic ion-cyclotron (EMIC) waves (Thorne and Kennel 1971). First studies of resonant interaction of relativistic electrons with EMIC waves have been within the framework of the quasi-linear theory (Summers and Thorne 2003; Jordanova et al. 2008; Shprits et al. 2009). In this approach, the waves are assumed to be noise-like broadband emissions, i.e., have incoherent phases, which allows one to describe the wave–particle interaction in terms of velocity-space diffusion. However, observation of quasi-monochromatic wave packets with short durations and large amplitudes from 1 to 14 nT (Kangas et al. 1998; Demekhov 2007; Engebretson et al. 2007, 2008; Pickett et al. 2010; Nakamura et al. 2019) inspired analysis of possible nonlinear resonant interaction and

*Correspondence: vsgrach@ipfran.ru
[1] Institute of Applied Physics of the Russian Academy of Sciences, Nizhny Novgorod, Russia
Full list of author information is available at the end of the article

its influence on precipitation (Albert and Bortnik 2009; Artemyev et al. 2015; Omura and Zhao 2012, 2013; Kubota and Omura 2017; Grach and Demekhov 2018a, b, 2020a). Also, there are observations of rapid loss of the outer radiation belt (Morley et al. 2010; Nakamura et al. 2019), which is too fast to be explained by quasi-linear diffusion rates, and thus requires nonlinear analysis.

Nonlinear theory of wave–particle interaction has been studied extensively for various wave modes (Karpman et al. 1974; Albert 1993, 2000; Shklyar and Matsumoto 2009; Albert and Bortnik 2009; Albert et al. 2012; Artemyev et al. 2015, 2017). The features of various interaction regimes were described analytically, including trapping by the wave field (Karpman et al. 1974; Albert 1993; Demekhov et al. 2006, 2009; Artemyev et al. 2015), phase bunching or nonlinear scattering (Albert 1993, 2000; Artemyev et al. 2017) and force bunching (Lundin and Shkliar 1977; Suvorov and Tokman 1988).

Wave–particle interaction with finite wave packets with various amplitude and frequency profiles has been studied mostly by test particle simulations (Tao et al. 2012; Omura and Zhao 2012, 2013; Chen et al. 2016; Kubota and Omura 2017; Zhang et al. 2018; Grach and Demekhov 2018a, b, 2020a; Zhang et al. 2020; Hiraga and Omura 2020). Regimes like directed scattering (Kubota and Omura 2017; Grach and Demekhov 2020a, b) or nonlinear shift of the resonance point (Grach and Demekhov 2020a) were revealed and analyzed. For whistler mode waves, it was shown that for realistic wave packets, nonlinear effects are much weaker than for single-frequency waves with a constant wave amplitude, because of the effects of amplitude modulation and short packet length (Tao et al. 2012; Zhang et al. 2018, 2020). On the other hand, the interaction with a chorus element, consisting of multiple subpackets, can still provide an effective acceleration (Hiraga and Omura 2020).

For EMIC waves, test particle simulations showed that resonant interaction of relativistic electrons with rising-tone EMIC wave packets can be very effective (Omura and Zhao 2012, 2013; Kubota and Omura 2017; Grach and Demekhov 2018b, 2020a). Precipitation flux in this case is heavily influenced and increased by nonlinear effects (Grach and Demekhov 2020a). (Chen et al. 2016) showed that sharp edges of the EMIC wave packets can lead to an effective nonresonant scattering of electrons with low energies.

Test particle simulations for resonant interaction with EMIC waves use model wave packets with main parameters based on observations. In particular, our previous paper (Grach and Demekhov 2020a) used model wave packets with linear frequency profile and two amplitude profiles, flat and Gaussian shaped. (Kubota and Omura 2017) used a more complicated structure with several subpackets but without direct correspondence to observational data.

Fine structure of a wave packet can play important role in the resonant interaction, both in linear and nonlinear regimes. In this paper, we study wave packets directly corresponding to Van Allen Probes (Mauk et al. 2013) observations. Specifically, we use the data for an event of 14 September 2017 observed by Van Allen Probe B.

Wave packet modeling

Data processing

We use high-resolution magnetic data of the Electric and Magnetic Field Instrument Suite and Integrated Science (EMFISIS) (Kletzing et al. 2013). The EMIC dynamic spectrum for Van Allen Probe B observations on 14 September 2017 is shown in Fig. 1a. We focus on rising-tone EMIC wave packets in proton band. Wave normal angles (not shown) are low, which is typical for EMIC waves (Loto'Aniu et al. 2005; Engebretson et al. 2007).

Discrete elements were identified using an algorithm developed by (Larchenko et al. 2019). The parameters of the algorithm were chosen so as to ensure 90 % of the wave packet energy $\int |B_{wf}|^2 \mathrm{d}f/(8\pi)$ to be confined in the detected elements (here $|B_{wf}|^2$ is the power spectral density (PSD) of the wave magnetic field and f is the wave frequency). The integration that is effectively replaced by summation over FFT frequencies is performed over the identified element range. Using such integration, we obtain instant amplitude B_w and frequency f of the wave packet: $B_w = \sqrt{\int |B_{wf}|^2 \mathrm{d}f}$, $f = \int |B_{wf}|^2 f \,\mathrm{d}f / B_w^2$.

We distinguished 31 isolated element (wave packet) and obtained their amplitude and frequency profiles (see Fig. 1b, c). The maximum wave amplitude is about 1.2–1.6 nT. Some of these elements can be considered isolated, some are overlapping in time and space. We divide 31 element into 12 groups, containing from 1 to 4 elements each and with duration from 40 to 250 s. We assume that each group corresponds to a fixed satellite location, and the plasma parameters stay constant during the generation, propagation and dissipation of elements in the group.

We assume that EMIC wave packets are generated in a small region near the equator, propagate along the geomagnetic field line and then dissipate in the He^+ cyclotron resonance region located father from the equator than the spacecraft. We use the dipole geomagnetic field model and obtain McIlwain parameter L using the satellite geomagnetic latitude λ_S and the measured geomagnetic field B_0. The gyrotropic model of the field-aligned profile of plasma density is used ($N_e \propto B_0$), and the measured local density is averaged over the group duration.

We study the wave–particle interaction with a single packet. For this study, we choose elements 14 and 22,

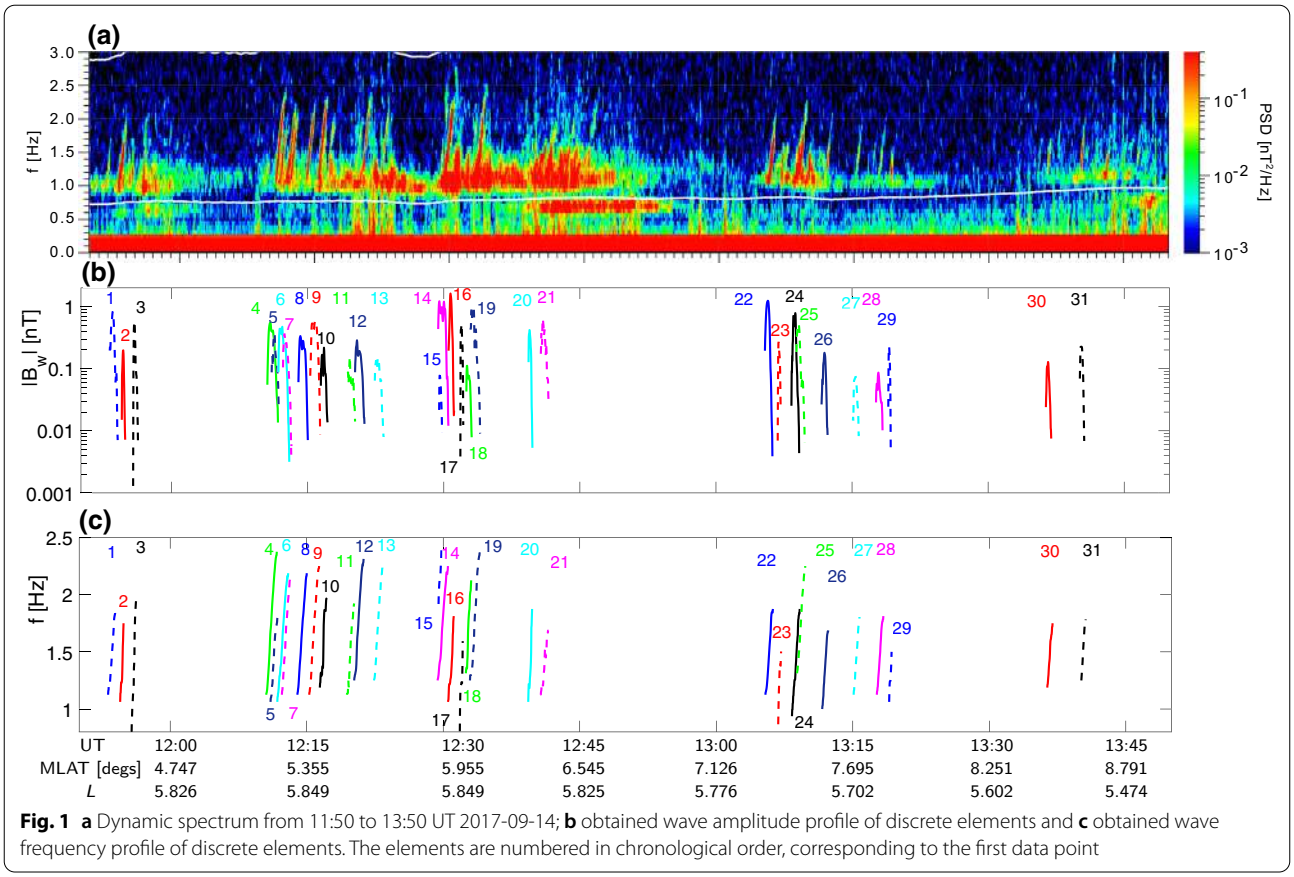

Fig. 1 **a** Dynamic spectrum from 11:50 to 13:50 UT 2017-09-14; **b** obtained wave amplitude profile of discrete elements and **c** obtained wave frequency profile of discrete elements. The elements are numbered in chronological order, corresponding to the first data point

which amplitudes are high enough for nonlinear interaction. The element 14 is overlapped with elements 15 and 16, but we neglect element 15 because of its small amplitude (the ratio of amplitudes $B_{w14}/B_{w15} = 10 \div 100$) and we will focus our study of element 14 on times before element 16 is generated.

The values of plasma parameters L, λ_S, N_e, corresponding to elements 14 and 22, are shown in Table 1. Hereafter, the subscripts L and S denote the values at the equator and at the spacecraft location, respectively. The other parameters, shown in Table 1, are discussed below.

Modeling of wave packet propagation

Propagation properties

We model the wave packet propagation in the geometrical-optics approximation, i.e., assume that each point propagates with a group velocity V_{gr} corresponding to the local dispersion relation and has its own frequency f that does not vary during the propagation: $\partial f/\partial t + V_{gr}(f)\partial f/\partial z = 0$ and amplitude B_w, which is discussed below.

We use the following additional simplifying assumptions for the wave generation and dissipation. (1) Each point of the packet starts at a single point $z_{start} < 0$ near the equator and propagates with increasing coordinate z along the geomagnetic field line ($z = 0$ corresponds to the equator). (2) The wave packet dissipates when it approaches the He^+ cutoff $z = Z_X(f)$ as detailed below. (3) We restrict the simulation parameters in such a way that the wave packet is not broken, i.e., the trajectories of its points do not intersect.

Table 1 Parameters for wave packet modeling

No.	λ_S	L	N_{eL}, cm^{-3}	N_{He}, %	N_O, %	z_{start}/z_d
14	5.9°	5.47	33.3	5.5	5.5	$-0.03R_E/0.51Z_X$
22	7.4°	5.39	33.5	7	7	$-0.1R_E/0.75Z_X$

To obtain the wave amplitude and frequency at an arbitrary point within the wave packet, we trace discrete points $j = 1 \ldots M$ (where $j = 1, M$ correspond to the leading and trailing edges of the packet, respectively) and interpolate between these points. Thus, we have the frequency profile $f_j(T_j)$ at the spacecraft location (see Figs. 2e and 3e). For each data point, we calculate the propagation "backwards" to z_{start} and thus obtain start times $t_j(f_j)$ for each traced point. Then, for each point, we calculate the propagation "forward" until the packet dissipates near cutoff location $Z_X(f_j) \equiv Z_{Xj}$.

For this approach to work, we have to place some restrictions on plasma composition, i.e., the He^+ density, to ensure the absence of wave packet breaking during the propagation. The dependence of group velocity V_{gr} on f/f_{He^+} (f_{He^+} is the local helium gyrofrequency) is non monotonic: V_{gr} decreases with f/f_{He^+} far from cutoff frequency and increases with f/f_{He^+} close to it. For a wave packet with strong enough negative frequency gradient (rising tone), the intersection of the trajectories (i.e, the amplitude profile breaking) is possible for the points with higher frequencies (trailing edge of the wave packet) when we calculate the propagation "backward" from the satellite to the equator. This happens if cutoff locations are too far away from the satellite location (N_{He^+} too low), thus decreasing of V_{gr} with f/f_{He^+} is too abrupt. On the other hand, when a wave packet with rising tone propagates "forward" away from the equator and nears the cutoff locations, the trajectories of the points with lower frequencies (leading edge of the wave packet) intersect, which leads to the wave packet distortion. This distortion cannot be correctly described by geometrical optics, so we need to gradually dissipate the wave packet, starting from the leading edge, before this distortion happens. For the model wave packet to correspond to satellite data, this dissipation should begin after the satellite location, which means that cutoff locations should not be too close to the satellite location (N_{He^+} cannot be too high). Thus, the value of N_{He^+} should be high enough that "backward" propagation from the satellite to the equator is possible without distortion and at the same time N_{He^+} should be low enough for the correct "forward" propagation from the equator to the satellite. The values for two considered wave packets are shown in Table 1. We also assume $N_{\text{O}^+} = N_{\text{He}^+}$.

Due to the properties of wave packet propagation, discussed above, "forward" propagation to the equator (from z_{start} to $z = 0$) without distortion is possible only in a small region. The values of z_{start} (chosen as the maximum

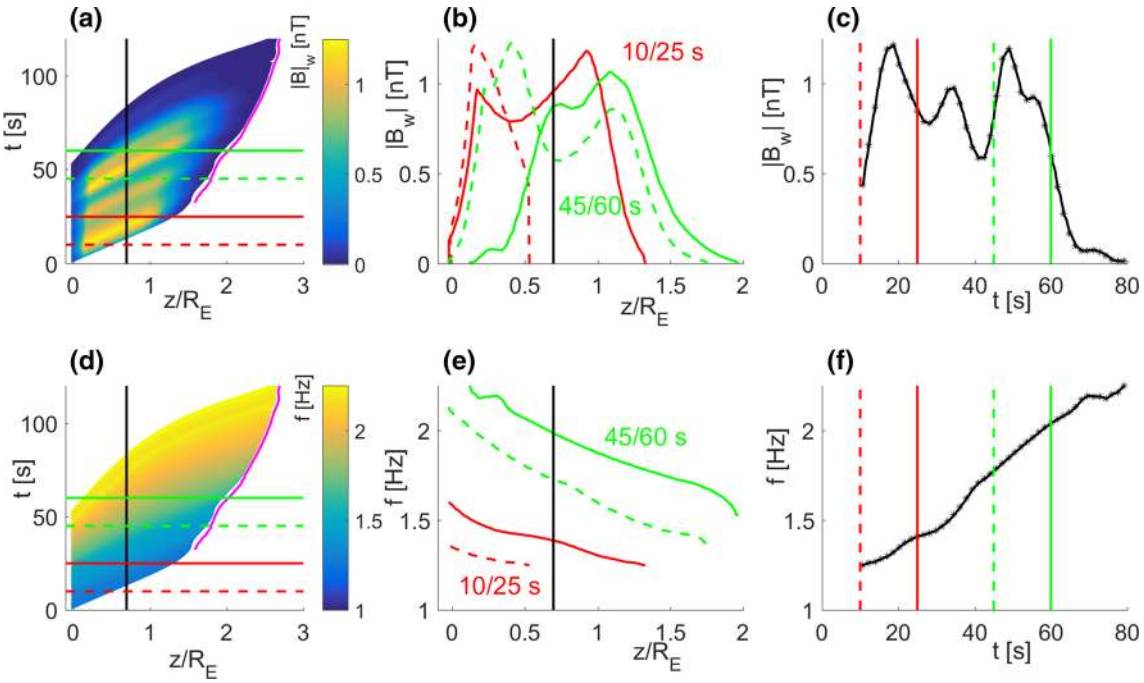

Fig. 2 Wave packet propagation for element 14: amplitude (**a**–**c**) and frequency (**d**–**f**) profiles. Panels **b** and **e** show spatial profiles at $t = 10$ s (dashed red line), 25 s (solid red line), 45 s (dashed green line) and 60 s (solid green line). Panels **c** and **f** show temporal profiles at the satellite location $z = z_S$ (black solid line), black markers represent the data from Fig. 1. Times 10; 25; 45 and 60 s are shown in panels **a**, **d** by horizontal lines and in panels **c**, **f** by vertical lines. Location $z = z_S$ is shown in panels **a**, **d**, **b**, **e** by vertical lines

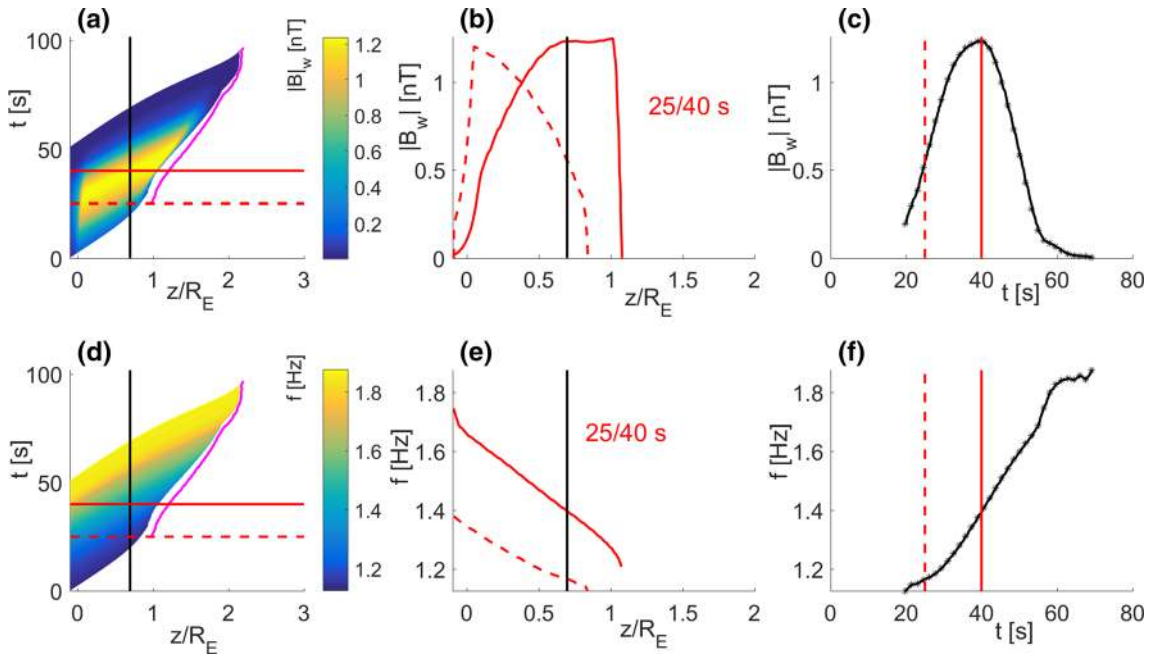

Fig. 3 Wave packet propagation for element 22: amplitude (**a**–**c**) and frequency (**d**–**f**) profiles. Panels **b** and **e** show spatial profiles at $t = 25$ s (dashed red line) and 40 s (solid red line). Panels **c** and **f** show temporal profiles at the satellite location $z = z_S$ (black solid line), black markers represent the data from Fig. 1. Times 25 and 40 s are shown in panels **a**, **d** by horizontal lines and in **c**, **f** by vertical lines. Location $z = z_S$ is shown in panels **a**, **d**, **b**, **e** by vertical lines

possible $|z_{\text{start}}|$) are also shown in Table 1 (hereafter, R_E denotes the Earth radius).

Amplitude and phase of the wave packet

We assume that there is a small region Δz_{gen} where the wave packet is generated (its energy increases), a small region Δz_{damp} where wave packet dissipates (its energy decreases, this region is located farther from the equator than the satellite) and in between for each point of the packet its energy flux $\mathcal{E} \propto B_w^2 V_{\text{gr}}/(8\pi)$ remains constant and corresponds to the satellite data. We choose the following model:

$$\mathcal{E}(f_j) = \begin{cases} \mathcal{E}_{\text{S}j}\delta_{\text{gen}} \exp[\eta_{\text{gen}j}(z - z_{\text{start}})], & z_{\text{start}} \le z \le z_{\text{c}j}; \\ \mathcal{E}_{\text{S}j}, & z_{\text{c}j} < z \le z_{\text{damp}j}; \\ \mathcal{E}_{\text{S}j} \exp[-\eta_{\text{damp}\,j}^2 (z - z_{\text{damp}\,j})^2], & z_{\text{damp}\,j} < z < \min\{0.99 Z_{X\,j}, z_{\text{cr}\,j}\}. \end{cases} \quad (1)$$

Here, $j = 1...M$, $z_{\text{cr}j}$ is the location of possible trajectory intersection, $\delta_{\text{gen}} = 1/50$, $\eta_{\text{gen}j} = -\ln \delta_{\text{gen}}/(z_{cj} - z_{\text{start}})$, $z_{cj} = z_{\text{start}} + \Delta z_{\text{gen}j}$, $\eta_{\text{damp}j}^2 = 5 \ln 10/(Z_{Xj} - z_{\text{damp}j})^2$.

We choose $\Delta z_{\text{gen}j} = 0.1 Z_{Xj}$, thus the generation region takes up to 10 % of the area of wave packet existence. The relation between z_{damp} and Z_X is chosen empirically for each wave packet, to ensure that wave amplitude is small enough at the dissipation point. The values of z_{damp} are shown in Table 1.

We also calculate the change in the wave phase for the leading and trailing edges of the packet:

$$\vartheta_j = \int k_j \mathrm{d}z - \int \omega_j \mathrm{d}t = \frac{\omega_j}{c} \int n_j \mathrm{d}z - \omega_j t. \quad (2)$$

Here, $\omega_j = 2\pi f_j$, k_j and n_j are wave number and refractive index for the frequency f_j, respectively. We set $\vartheta_j = 0$ at $z = z_{\text{start}}$ for any j.

While the packet is generated, the trailing edge of the packet is located at z_{start} and so the phase of the trailing edge $\vartheta_{\text{te}} = 0$. Once the generation is finished, $\vartheta_{\text{te}} = \vartheta_M$ and changes smoothly. On the contrary, the phase of the leading edge changes smoothly at first, while $\vartheta_{\text{le}} = \vartheta_1$, then, once the packet starts to dissipate, $\vartheta_{\text{le}} = \vartheta_j$, where j increases (the leading edge frequency increases until the packet dissipates completely).

The results of wave packets modeling are shown in Figs. 2 and 3. Hereafter, time t starts at the generation moment of the leading edge of the packet.

As one can see from Figs. 2,3, all the frequencies which can be seen in satellite data do not exist at the same time. By the time the wave with the highest frequency in the packet (trailing edge) is generated, the waves with lowest frequencies (leading edge) have been already dissipated at the He^+ resonance. This means that any spatial distribution will contain only part of the frequency spectrum.

Wave–particle interaction: theory

Basic equations

The resonant interaction with parallel-propagating EMIC waves is possible only for relativistic electrons and at the anomalous cyclotron resonance. The resonance condition is written as follows:

$$\Delta = \omega - k v_{||} + \Omega_c/\gamma = 0, \tag{3}$$

where ω and k are wave frequency and number, respectively, $v_{||}$ is field-aligned velocity, $\Omega_c = eB_0/mc$, B_0 is geomagnetic field, $e > 0$ is elementary charge, $\gamma = \sqrt{1 + [p/(mc)]^2}$, m and p are the electron rest mass and momentum, respectively.

We use the same equations of motion for test electrons interacting with EMIC waves as (Grach and Demekhov 2020a):

$$\frac{dW}{dt} = -ev_{\perp}|E_w| \sin\Psi; \tag{4}$$

$$\frac{dI_{\perp}}{dt} = -\frac{2e}{mB_0} p_{\perp}(1 - n_{||}\beta_{||})|E_w| \sin\Psi; \tag{5}$$

$$\frac{d\Psi}{dt} = -\Delta - \frac{e}{p_{\perp}}(1 - n_{||}\beta_{||})|E_w| \cos\Psi; \tag{6}$$

$$\frac{dz}{dt} = \frac{p_{||}}{m\gamma}. \tag{7}$$

Here, the subscripts $||$ and $\perp$ denote projections to the parallel and transverse directions with respect to $\mathbf{B}_0$, respectively, E_w is slowly changing wave electric field amplitude, $n_{||} = kc/\omega$, $\Psi = \vartheta - \varphi$, φ is the gyrophase in the geomagnetic field $\mathbf{B}_0$, ϑ is the wave phase, $\beta_{||} = v_{||}/c$, $W = (\gamma - 1)mc^2$ and $I_{\perp} = p_{\perp}^2/(mB_0)$ are the electron kinetic energy and the first adiabatic invariant respectively, and z is coordinate along the geomagnetic field with $z = 0$ corresponding to the equator. In the right-hand side of equation (5), the first term represents inertial, or kinematic bunching, while the second one represents the direct influence of Lorentz force on the particle phase (force bunching).

In (4)–(7) it is assumed that the external field inhomogeneity is smooth, the wave magnetic field amplitude is small ($B_w \ll B_0$) and wave characteristics vary slowly in time and space on the scales of $2\pi/\Omega_c$ and $2\pi/k$, respectively.

For EMIC waves $\omega \ll \Omega_c$, and thus the resonant interaction is possible only for $k_{||}v_{||} > 0$ and the change in electron energy W will be insignificant: $\gamma \approx$ const (Bespalov and Trakhtengerts 1986; Albert and Bortnik 2009). The interaction result is described by the change in the adiabatic invariant $I_{\perp}$ or equatorial pitch angle Θ_L, $\mu = \sin^2\Theta_L = (p_{\perp}^2/p^2)(B_L/B_0)$.

Summary of earlier analytical results

For the reader's convenience, we briefly summarize earlier results of various authors (Karpman et al. 1974; Albert 1993, 2000; Albert and Bortnik 2009; Kubota and Omura 2017; Grach and Demekhov 2018a, 2020a).

Particle behavior during the interaction (interaction regime) is determined by the inhomogeneity parameter $\mathcal{R} = \sigma_R R$ (Karpman et al. 1974; Albert 1993, 2000; Albert and Bortnik 2009; Kubota and Omura 2017; Grach and Demekhov 2018a), where $\sigma_R = \pm 1$ determines the effective inhomogeneity sign, and

$$R = \frac{|d\Delta/dt|}{\Omega_{tr}^2}. \tag{8}$$

Here, the time derivative $d/dt = \partial/\partial t + V_{||}\partial/\partial z$ represents the full change along the electron orbit with differentiating only on functions z and t, excluding W and $I_{\perp}$; $\Omega_{tr}^2 = (1 - n_{||}^{-2})e\omega n_{||}^2 v_{\perp}|E_w|/(mc^2\gamma)$ is the frequency of electron oscillations in the wave field near the effective potential minimum (Grach and Demekhov 2018a; Demekhov et al. 2006). Under real conditions, the parameter R changes both in time and in space. These changes are associated both with medium inhomogeneity (including changes in the wave packet frequency and amplitude) and nonlinear changes in the particle parameters during the interaction. However, the main features of the particle motion can be categorized based on the R values calculated at the resonance point in the linear approximation. For $R > 1$, the trajectories of all particles on the phase plane are open (all particles are untrapped), and for $R < 1$, there is a minimum of the wave effective potential, i.e., particle trapping by the wave field is possible. The phase trajectories of the trapped particles are closed. For resonant interaction of electrons with EMIC wave packet, which is generated near the equator and propagates away from it, the effective inhomogeneity is negative. Hereafter, we assume $\sigma_R = -1$.

The case of $R \gg 1$ corresponds to the linear regime. In this case, the change in particle equatorial pitch angle depends on initial phase. For an ensemble of particles with the same initial equatorial pitch angle and initial phases uniformly distributed in $[0, 2\pi)$ pitch angle diffusion takes place (Albert 2000; Albert and Bortnik 2009; Grach and Demekhov 2018a, 2020a):

$$\langle \Delta\mu \rangle^{\mathrm{lin}} = 0; \tag{9}$$

$$\sqrt{\langle (\Delta\mu^{\mathrm{lin}} - \langle \Delta\mu \rangle^{\mathrm{lin}})^2 \rangle} = \sigma_\mu^{\mathrm{lin}} > 0. \tag{10}$$

Hereafter, angle brackets denote averaging over initial phases of the considered particle ensemble. The root mean square deviation σ_μ determines the diffusion coefficients in the linear regime.

For $R \leq 1$, the resonant interaction is nonlinear, which leads to drift in pitch angles for both trapped and untrapped particles. For relativistic electrons interacting with EMIC waves, propagating away from the equator, trapping can lead to a significant decrease in pitch angle (Albert and Bortnik 2009; Kubota and Omura 2017; Grach and Demekhov 2018a, 2020a). For most of the untrapped particles, phase bunching without trapping or nonlinear scattering takes place (Albert 1993, 2000; Artemyev et al. 2017), which leads to pitch angle increase (Albert and Bortnik 2009; Grach and Demekhov 2018b, 2020a). When $R < 1$ is not too small, directed scattering, which leads to a significant pitch angle decrease, is possible for a small group of untrapped particles (Kubota and Omura 2017; Grach and Demekhov 2018a, 2020a).

Nonlinear effects can also take place for not too high $R \geq 1$. If the wave amplitude is high enough, then the region of resonant interaction is large and the exact resonance point is shifted during the interaction. It leads to particles with the same initial pitch angle but different initial phases having different resonance points, and, consequently, different values of R. For an individual particle, $|\Delta\mu|$ in the linear regime depends on both the R value and the initial phase, while the sign of $\Delta\mu$ is determined only by phase. Thus, for example, if R decreases with μ, then for particles with initially increasing μ the change $|\Delta\mu|$ will be bigger than for particles with initially decreasing μ. So, when the dependence $R(\mu)$ is significant, the nonlinear shift of the resonance point causes drift in μ ($\langle \Delta\mu \rangle \neq 0$, see (Grach and Demekhov 2020a) for more details).

Force bunching (the Lorentz force term in Eq. (5) for the particle phase, which is neglected in linear approximation) becomes significant for particles with low Θ_L. It was shown analytically by (Lundin and Shkliar 1977) that force bunching leads to systematic increase in electron pitch angle for resonance electrons with low transverse velocities in the field of a whistler mode parallel propagating wave. Lately, numerical simulations showed similar results for electrons interacting with EMIC waves (Grach and Demekhov 2020a), right-hand extraordinary mode (Grach and Demekhov 2020b), and whistler waves (Kitahara and Katoh 2019; Gan et al. 2020). The significance of force bunching term has also been proven for electron dynamics upon cyclotron resonance breakdown and heating in laboratory mirror traps by high-power microwaves (Suvorov and Tokman 1988). For EMIC waves, it was showed in (Grach and Demekhov 2020a) that force bunching can completely block precipitation from low pitch angles close to the loss cone.

Wave–particle interaction: numerical calculations

The system (4)–(7) was solved numerically by Bogacki–Shampine variant of the Runge–Kutta method. The wave field $E_{\mathrm{w}}(z,t) = B_{\mathrm{w}}(z,t)/n_{||}(z,t)$ and frequency $\omega(z,t) = 2\pi f(z,t)$ are calculated beforehand according to the wave packet model described above (see Figs. 2, 3). When the particle is outside the wave packet, its energy $\mathcal{W}$ and adiabatic invariant $I_\perp$ remain constant and only gyrophase φ and particle location z change. The phase Ψ on the particle next entrance in the packet is calculated taking into account the increments both in φ and in the wave phase ϑ for the packet edges (ϑ_{le} and ϑ_{te}, see (2)). The wave packet at any given time is short enough, so that its evolution (generation, propagation and dissipation) during the single pass of the particle through it is negligible, but it becomes significant over several bounce oscillations.

For every energy, calculations were done for 82 values of equatorial pitch angle (range 4°–85°, step of 1 degree) and 360 values of the initial phase (uniformly in $[0, 2\pi)$). Thus, for every energy, the trajectories of 29520 particles were calculated. We assume particle energies $1\ \mathrm{MeV} \leq W_0 \leq 10\ \mathrm{MeV}$. At the beginning of simulation $t = t_{\mathrm{begin}}$ all particles are placed at the point $z = -0.1R_{\mathrm{E}}$ with positive longitudinal velocities. As is shown below, this is insignificant for the results, since the particles are spread over the field line in 4–8 bounces. If a particle is in the loss cone after leaving the packet ($\Theta_L < \Theta_{Lc}$), then the simulation for this particle is stopped. For both considered sets of plasma parameters, the equatorial pitch angle, corresponding to the loss cone, $\Theta_{Lc} \approx 3.4°$.

Preliminary analysis of resonance conditions

Our simulation model, based on Eqs. (4)–(7) and independently calculated wave packets, shown in Figs. 2 and 3, does not take into account the effect of magnetic drift on the electron distribution function in a given flux tube. To justify this approximation, we must limit our simulation to times which do not exceed drift times across

the wave packet. These times are significantly shorter than 100–120 s of wave packets existence (specific values are discussed below). To determine simulation time and range of test particle energies, we first analyze resonant conditions for the considered wave packets and the behavior of inhomogeneity parameter R unperturbed values.

If the frequency range of the wave packet remains constant during the simulation, we can analyze resonant conditions for the single pass through the wave packet near the equator and then predict their behavior during wave packet propagation (Grach and Demekhov 2018a, 2020a). With lower-frequency waves dissipating and higher-frequency waves generating during possible simulation time (see bottom panels of Figs. 2 and 3), we have to analyze resonance points and R values at these points for the whole time when the wave packet exists.

In Fig. 4a, the distribution of resonance points with $R < 10$ over time is shown for both wave packets. In Fig. 4b and c, we show time dependencies of minimum R values over the trajectory (for $R_{\min} \leq 5$). Based on these calculations and several test simulations we choose three cases for our further simulations: (I) element 14, time interval 10–25 s; (II) element 14, time interval 45–60 s; (III) element 22, time interval 25–40 s. Dependencies of $R_{\min}(\Theta_{L0}, W_0)$ for these three cases are shown at bottom panels of Fig. 4. These intervals correspond to the most effective wave–particle interaction and represent all the possible interaction regimes. Note that taking into account wave packet dissipation in the He^+ cyclotron resonance region allowed us to use longer simulation time than in (Grach and Demekhov 2020a) (15 s instead of 6.5 s).

These time intervals are shown in Figs. 2 and 3, as well as spatial profiles of wave amplitude and frequency at the start and end of the intervals (hereafter, t_{begin} and t_{end}, respectively). As one can see from the Figures, Case I (element 14, time interval 10–25 s) corresponds to the biggest changes in the packet length during the interaction interval. We can also see that in Case I there is an active generation of higher-frequency waves at the trailing edge during the simulation time but dissipation of lower-frequency waves at the leading edge does not take place. Case II (element 14, time interval 45–60 s) corresponds to the widest frequency range (1.4–2.35 Hz) and to the longest wave packet spatial structure (close to $2R_E$). Generation of the packet is mostly finished by the beginning of Case II, but dissipation of lower-frequency waves has started. Case III (element 22, time interval 25–40 s) corresponds to the strongest increase in frequency; both generation and dissipation take place during the simulation time.

The highest frequencies in Case II result in the lowest resonant energies (see Fig. 4e). We also can see that Case II has the largest range of resonant pitch angles and the widest area of possible nonlinear interaction

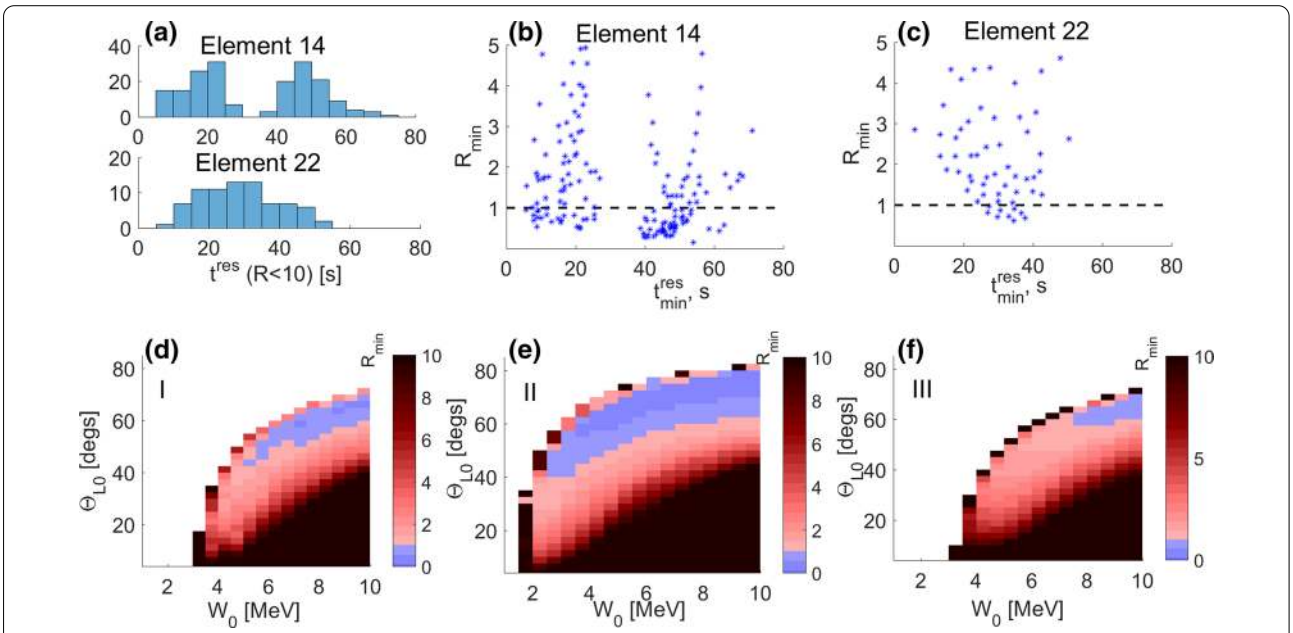

Fig. 4 Resonance conditions. Distribution of resonance points with $R < 10$ over time (**a**) and dependencies of $R_{\min} \leq 5$ on time (**b**, **c**) for the whole packet. Dependencies $R_{\min}(\Theta_{L0}, W_0)$ for the chosen time intervals: element 14, 10–25 s (case I, **d**), element 14, 45–60 s (case II, **e**), element 22, 25–40 s (case III, **f**). On the bottom panels the $R_{\min}$ scale is limited by $R = 10$

(corresponding to lower R values). It is noteworthy that the zone of resonant interaction is determined by the effective wave packet length for the considered packets, since the zone determined by the phase mismatch is wider.

The calculations were done in the following energy ranges: 3.5 ÷ 8.0 MeV for Case I, 1.5 ÷ 5.5 MeV for Case II and 3.5 ÷ 9.0 MeV for Case III, with steps of 0.5 MeV. Here, the lower limit corresponds to the lowest energy for which the range of resonant pitch angles exceeds 20°, the upper limit is chosen based on test estimates on precipitation flux (see below).

For particles with maximum considered energy 9 MeV the chosen simulation duration of 15 s corresponds to the drift time across an arc of 5°, which seems reasonable transverse size for an EMIC wave packet. For longer time intervals, drift effects have to be taken into account. The chosen time interval 15 s corresponds to 25–50 bounce periods.

Interaction regimes

First, we study which interaction regimes are possible for the considered wave packets and particle ensemble, and how their features depend on particle parameters and wave packet evolution.

In this section, we analyze the interaction regimes based on phase averaged change in $\mu = \sin^2\Theta_L$ after a single pass through wave packet for given W_0, Θ_L and time. Significant $\langle\Delta\mu\rangle \neq 0$ will allow us to determine a predominant nonlinear regime: $\langle\Delta\mu\rangle > 0$ corresponds to either force bunching, nonlinear shift of the resonance point (lower Θ_L) or phase bunching, $\langle\Delta\mu\rangle < 0$ corresponds to either nonlinear shift of the resonance point (higher Θ_L) or trapping (Grach and Demekhov 2020a).

To calculate $\langle\Delta\mu\rangle$ at a time t for every $\Theta_L = 4°, 5°, ..., 85°$ we find all test particles outside the wave packet with equatorial pitch angle $\Theta_L^* \in [\Theta_L - 0.5°, \Theta_L + 0.5°]$. Then, change in μ for these particle after their next pass through the wave packet is averaged over initial phases, and thus we obtain $\langle\Delta\mu\rangle$ and rms σ_μ as a function of Θ_L.

In Fig. 5, we plot $\langle\Delta\mu\rangle(\Theta_L)$ and $\sigma_\mu(\Theta_L)$ for two moments during the simulation and three values of electron energy W_0 for all three cases (here Θ_L is the equatorial pitch angle before the pass through the packet).

The dependencies $\langle\Delta\mu\rangle(\Theta_L, W_0)$, $\sigma_\mu(\Theta_L, W_0)$ are similar for all three cases and are also in agreement with previous results for model wave packets with Gaussian amplitude profile (Grach and Demekhov 2020a).

For lower energies (close to the lower limit of the resonant range, top row in Fig. 5) small positive maximum of $\langle\Delta\mu\rangle$ at smaller Θ_L is related to force bunching, with small influence of nonlinear shift of the resonance point. The negative minimum of $\langle\Delta\mu\rangle$ at higher Θ_L is also caused by nonlinear shift of the resonance point (trapping by the wave field is not possible at these energies, see Fig. 4). For higher energies (close to the upper limit of the resonant range, bottom row in Fig. 5), positive maximum of $\langle\Delta\mu\rangle$ is located at intermediate Θ_L and caused by a nonlinear shift of the resonance point with a small influence of phase bunching. A strong negative minimum near the upper limit of resonant range of Θ_L is related to the particle trapping by the wave field. The nonlinear effects are the strongest ($|\langle\Delta\mu\rangle| \geq \sigma_\mu$) for lower energies and low pitch angles close to the loss cone and for trapping (Case II, higher energies). For higher energies and relatively wide range of $\Theta_L < 25°$–$40°$, the interaction is linear ($\langle\Delta\mu\rangle(\Theta_L) \approx 0$) with small rms deviation σ_μ (and, consequently, small diffusion coefficients).

With increasing energies (from top row to bottom in Fig. 5), the extrema of $\langle\Delta\mu\rangle(\Theta_L)$ are shifted to the higher values of Θ_L.

The influence of complicated packet structure (in comparison with simpler models (Grach and Demekhov 2018b, 2020a)) can be seen in the temporal dynamics of the dependencies $\langle\Delta\mu\rangle(\Theta_L), \sigma_\mu(\Theta_L)$, because this dynamics is mostly determined by the wave packet evolution. For dependencies $\langle\Delta\mu\rangle(\Theta_L)$, only Case II shows roughly the same temporal dynamics as the model wave packets, considered in (Grach and Demekhov 2018b, 2020a): $|\langle\Delta\mu\rangle(\Theta_L)|$ decreases with time, and the extrema of $\langle\Delta\mu\rangle(\Theta_L)$ are shifted to the lower values of Θ_L. For Cases I and III, $|\langle\Delta\mu\rangle(\Theta_L)|$ can either increase or decrease and the extrema of $\langle\Delta\mu\rangle(\Theta_L)$ are shifted to the higher values of Θ_L.

This dynamics is explained as follows. For electrons with lower energies and/or higher pitch angles (corresponding to exrema in $\langle\Delta\mu\rangle(\Theta_L)$), the resonance points are located closer to the trailing edge. Therefore, the resonant interaction with these particles will be strongly influenced by generation of higher-frequency waves at the packet trailing edge near the equator. For Case II, the generation of higher-frequency waves during the simulation time is not significant (see Fig. 2): generation stops in the middle of the simulation, the increase of trailing edge frequency is small and the amplitudes of the generated waves are low. Thus, evolution of $\langle\Delta\mu\rangle(\Theta_L)$ in Case II is caused mostly by wave packet propagation, like in (Grach and Demekhov 2020a). On the contrary, for Cases I and III, generation of higher-frequency waves at the equator during the simulation time plays an important role in the packet evolution and temporal dynamics of wave–particle interaction (see Figs. 2,3).

Temporal dynamics of $\sigma_\mu(\Theta_L)$ in the linear regime at low Θ_L is also different for different cases (see bottom row of Fig. 5): σ_μ increases with time in Case I, decreases only slightly in Case II and remains constant in Case III.

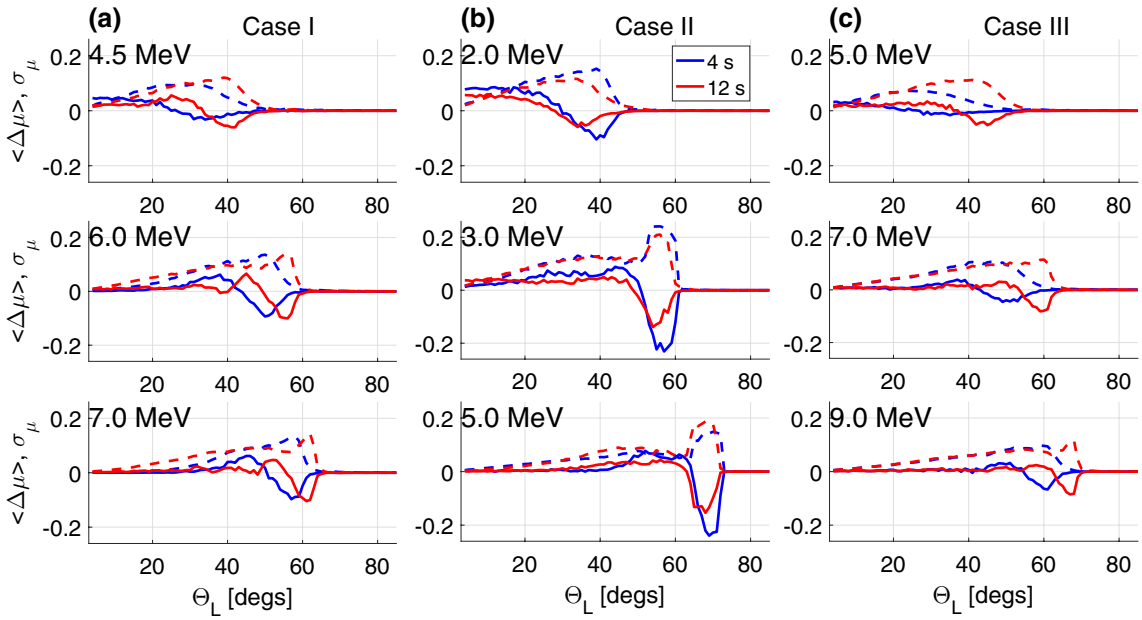

Fig. 5 Phase averaged change in μ (solid lines) and root mean square deviation σ_μ (dashed lines) for different energies for Case I (**a**), II (**b**) and III (**c**) for $t - t_{\text{begin}} = 4$ s and $t - t_{\text{begin}} = 12$ s (blue and red lines, respectively)

The results of (Grach and Demekhov 2020a), on the contrary, show only an increase in σ_μ with time for low pitch angles and higher energies (see Appendix there). The reason for such a difference stems from the fact that the resonance points of such electrons are located near the leading edge of the packet (Grach and Demekhov 2018b, 2020a). So, the resonant interaction with these particles will be influenced by the dissipation of lower-frequency waves once the packet nears He^+ resonance. In Case I, there is no dissipation during the simulation time; so, σ_μ increasing is due to wave packet propagation, like in (Grach and Demekhov 2020a). In Cases II and III, $\sigma_\mu(\Theta_L)$ temporal dynamics is determined by the wave packet dissipation, though amplitude modulation also can have a quantitative effect.

We should also note that particle trapping by the wave field leads to a significant change in Θ_L (up to 40°) only in Case II (the case with minimum values of inhomogeneity parameter R and the longest packet). In Cases I and III, pitch angle change as a result of trapping does not exceed 20°, mostly because effective packet lengths are shorter in these cases. The similar results of particles detrapping due to short packet effective lengths were observed in test particle simulations for whistler mode packets (Tao et al. 2012).

Precipitation mechanisms

Let us analyze particle precipitation mechanisms during the entire simulation time. Following (Grach and Demekhov 2020a), we plot the scattering pitch angle Θ_{Lsc} (equatorial pitch angles of precipitating electrons before the last interaction with the wave packet) as a function of time. Figure 6 shows the results for Case II, and the results for the other two cases are qualitatively similar.

As one can see from Fig. 6, the maximum scattering pitch angle Θ_{Lsc} is about 30°. According to previous analysis (see Figs. 4, 5 and relevant discussion), for these pitch angles $R > 1$. Thus, of nonlinear regimes only force bunching and/or nonlinear shift of the resonance point are possible.

Force bunching blocks precipitation from low pitch angles for lower energies (about one half of the considered energy range). At the same time, when precipitation from low Θ_L is blocked by force bunching, it is possible from higher Θ_L. Specifically, at $W_0 = 2$ MeV (Fig. 6b), precipitation is blocked from $\Theta_{Lsc} \le 20°$ (at early times) but is possible from Θ_{Lsc} up to 30°. This precipitation occurs in the regime which is close to linear (with small influence of nonlinear shift of the resonance point). For higher energies, when the effect of force bunching is absent (Fig. 6e and f), $\Theta_{Lsc} \le 10°$. The range of blocked pitch angles and maximum Θ_{Lsc} have a maximum over energy; for entirely linear precipitation the range of Θ_{Lsc} decreases with energy.

Trapping by the wave field cannot directly cause precipitation, because it occurs at high pitch angles and $|\Delta\Theta_L| < \Theta_{L0} - \Theta_{Lc}$. To analyze indirect influence of trapping, we plot the maximum change (decrease)

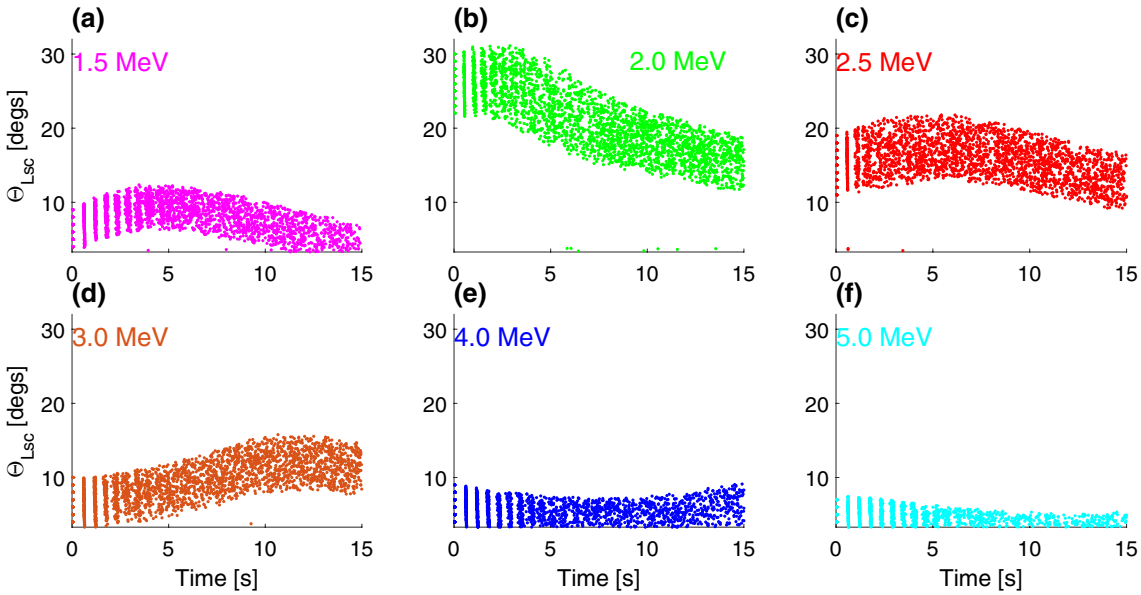

Fig. 6 Equatorial pitch angles Θ_{Lsc} of precipitating electrons before the last interaction with the wave packet as a function of time for Case II. Time is counted from the beginning of simulation and corresponds to particle exiting the wave packet

in Θ_L of precipitating particles over their trajectories $|\Delta\Theta_L|^{\text{lost}}_{\text{max}}$. The results for Case II are shown in Fig. 7. For lower energies (Fig. 7a and b) the trapping is impossible (see Fig. 4e), and $|\Delta\Theta_L|^{\text{lost}}_{\text{max}}$ has roughly the same value as the change which leads directly to precipitation. For intermediate energies (Fig. 7c and d) particles that have been trapped along their trajectory can make up a significant part of precipitating particles. For higher energies (Fig. 7f), there are no trapped particles in the loss cone, despite the fact that for these energies trapping is the most effective. It happens because trapping takes place for $\Theta_L \geq 60°$, while in rather wide range $\Theta_L \leq 40°$ the wave–particle interaction is linear with small σ_μ (see bottom row of Fig. 5). Thus, trapped particles do not have enough time to reach the loss cone due to diffusion after they leave the trapping region.

Figures 6 and 7 also demonstrate the influence of the initial particle distribution in space at the beginning of the simulation. As one can see, this influence disappears after $4-8$ bounce oscillations (approximately $2-5$ s).

Temporal dynamics of Θ_{Lsc} is complicated, different for different energies even within one case and more diverse than for a model packets considered in (Grach and Demekhov 2020a). When nonlinear effects are strong ($W_0 < 4$ MeV, Fig. 6a–d), the difference from the earlier results is mostly due to longer simulation time. When precipitation is linear or almost linear ($W_0 \geq 4$ MeV, Fig. 6e and f), the range of precipitation pitch angles has a slight minimum or decreases with time; for a model wave packet with Gaussian amplitude profile, precipitation pitch angle range increases with time for linear precipitation (Grach and Demekhov 2020a).

This difference is explained by the fact that for particles with higher energies and low pitch angles resonant interaction is influenced by dissipation of the lower-frequency waves once the packet nears the He^+ resonance. Also, spatial amplitude profiles for Case II are different from Gaussian one (see Fig. 2b); this amplitude modulation is not strong enough to cause qualitative difference for interaction regimes at any given time, but can have quantitative effect.

For Cases I and III, generation of higher-frequency waves might influence Θ_{Lsc} temporal dynamics. These dynamics is roughly the same as temporal dynamics of precipitating flux, that is discussed below.

Evolution of the distribution function

To analyze the simulation results in terms of particle distribution function and for correct analysis of precipitating fluxes, we have to establish the connection between the distribution function $\Phi_{\Theta_L}(\Theta_L)$ and the distribution of the test particles in the phase space. As in (Grach and Demekhov 2020a) we use the following normalization (Bespalov and Trakhtengerts 1986; Trakhtengerts and Rycroft 2008):

$$N = \int n(z) \frac{B_{0\text{m}}}{B_0(z)} \mathrm{d}z. \tag{11}$$

Here, N is the number of particles in a geomagnetic flux tube with a unit cross section at the ionosphere,

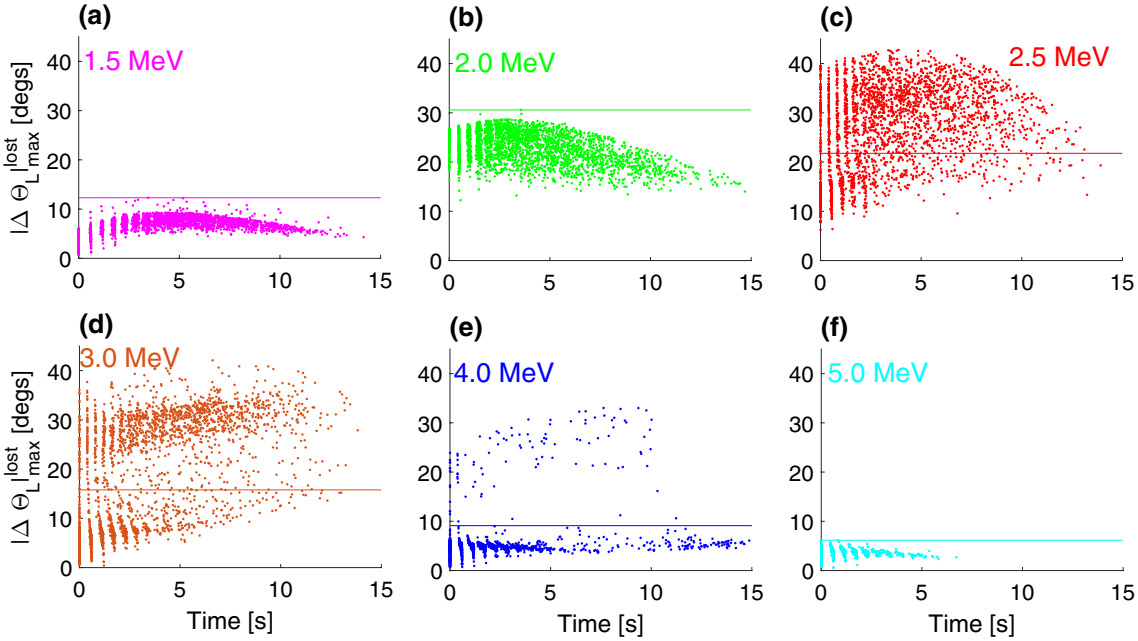

Fig. 7 The maximum change in equatorial pitch angle over the trajectory for precipitating electrons. Case II, time is counted from the beginning of simulation and corresponds to particle exiting the wave packet after the maximum change has occurred. Horizontal line shows the maximum change for the precipitation itself

$n(z) = \int f d^3\mathbf{p} = \int f \sin\Theta \mathrm{d}\Theta\, p^2 \mathrm{d}p\, \mathrm{d}\Psi$ is the local number density, f is the local particle distribution function averaged over gyrophases, Θ is the local pitch angle, p is particle momentum and $B_{0\mathrm{m}}$ is the maximum field for the given geomagnetic field line. The distribution function f can be averaged over bounce oscillations and integrated over particle momentum (taking into account that the electron energy is conserved with a high accuracy) and over phases and thus, we obtain particles distribution in equatorial pitch angles $\Phi_{\Theta_L}(\Theta_L)$.

We can also express N via the number of test particles in the simulation, N_p:

$$N = \frac{v_0 \overline{T}_B}{2\mu_\mathrm{c}} \beta_\mathrm{V} N_\mathrm{p}, \tag{12}$$

where v_0 is particle velocity (which stays constant during the interaction), $\mu_\mathrm{c} = \sin^2\Theta_{Lc}$ corresponds to the loss cone, $\overline{T}_B = \int T_\mathrm{B}(\mu)\mathrm{d}\mu$, β_V is the normalization constant, and N_p is the number of test particles in the simulation.

Using (11) and (12), we can write the connection between distribution function Φ_{Θ_L} and distribution of the test particles in the phase space as follows:

$$\Phi_{\Theta_L} = \frac{\Delta N_\mathrm{p}}{\Delta\Theta_L} \frac{\overline{T}_B}{T_\mathrm{B}} \frac{\beta_\mathrm{V}}{\sin(2\Theta_L)}. \tag{13}$$

Here ΔN_p is the number of test particles having the pitch angle Θ_L within the range $\Delta\Theta_L$.

We also assign a specific weight to each test particle to ensure that the initial particle distribution $\Phi_{\Theta_L}|_{t=t_\mathrm{begin}}$ is constant. More details can be found in the Appendix of (Grach and Demekhov 2020a).

We divide the total simulation time 15 s in 26 intervals $\{\Delta t_i\} = t_{i+1} - t_i$, $i = 0, 1, ..., 26$, $t_0 = t_\mathrm{begin}$, $t_{26} = t_\mathrm{end}$, where $\Delta t_0 = \Delta t_{25} = 0.3$ s and the other intervals $\Delta t_{0<i<25} = 0.6$ s. The value 0.6 s corresponds to the bounce period of particles close to the loss cone: $T_\mathrm{B}(\Theta_L = \Theta_{Lc}) \approx 0.6$–$0.62$ s. The first interval is chosen shorter, because at $t_0 = t_\mathrm{begin}$ the particle ensemble is located near the equator; the time $\Delta t_0 = 0.3$ s is long enough that all particles precipitated after the first pass through the packet will reach the ionosphere and short enough that all other particles during Δt_0 will pass the wave packet in the resonant direction only once. In the further analysis, both Δt_0 and Δt_{25} will be ignored.

We average the particle distribution function over the intervals Δt_i and attribute the obtained result to the time $\tau_i = (t_{i+1} + t_i)/2$ (the middle of the interval Δt_i). We use the grid in Θ_L which is not fine enough to ensure distribution function resolution within the loss cone, so in the loss cone the distribution function has one value, $\Phi^\mathrm{c}_{\Theta_L}$.

Figure 8 shows the evolution of distribution function for 3 values of energy in Case II. These energies represent

three typical patterns of wave–particle interaction in Case II; Cases I and III also demonstrate the similar patterns.

For $W_0 = 2$ MeV (lower energies), the distribution function is close to isotropic for $\Theta_L \leq 60°$ (there is no resonant interaction for higher Θ_L, so the distribution function remains undisturbed). The value of Φ_{Θ_L} slowly decreases with time from the initial value $\Phi^0_{\Theta_L}$ to approximately $0.8\Phi^0_{\Theta_L}$.

For $W_0 = 3$ MeV (intermediate energies), the distribution function is close to isotropic up to $\Theta_L \approx 20°$–$30°$ and then there are noticeable variations with a maximum in the vicinity of 40° and a minimum in the vicinity of 50°. These variations are caused by phase bunching and trapping.

For $W_0 = 5$ MeV (higher energies), the distribution function increases from $\Phi^c_{\Theta_L} \approx (0\text{–}0.5)\Phi^0_{\Theta_L}$ in the loss cone to the initial value $\Phi^0_{\Theta_L}$ at $\Theta_L \approx 20°$. Noticeable variations, associated with phase bunching and trapping by the wave field, take place in the area $\Theta_L \approx 40°$–$70°$ and thus do not influence the precipitation.

The behavior of the distribution function in the vicinity of the loss cone is roughly the same as for the model Gaussian packet in (Grach and Demekhov 2020a). Trapping by the wave field is not effective for Gaussian packet and particle ensemble considered in (Grach and Demekhov 2020a), so noticeable variations, associated with trapping, were present only for a model packet with flat amplitude profile.

Precipitating flux

For the further analysis, we normalize the precipitating fluxes $S^{\rm num}_{\rm pr}$, directly corresponding to the numerical simulation results, to the flux $S^{\rm SD}_{\rm pr}$ in the limiting case of strong diffusion. In this case the loss cone is filled continuously and distribution function is isotropic; the precipitating flux takes the limiting value equal to the trapped flux (Kennel and Petschek 1966; Bespalov and Trakhtengerts 1986; Trakhtengerts and Rycroft 2008):

$$S^{\rm SD}_{\rm pr} = \frac{N\mu_c}{\overline{T}_B}. \tag{14}$$

Here N is the number of particles in geomagnetic field tube with a unit cross section at the ionosphere (11), (12). The simulated precipitating flux is evaluated as:

$$S^{\rm num}_{\rm pr}(\tau_i) = \frac{N\delta N_{\rm p}}{\Delta t_i}. \tag{15}$$

Here, $\delta N_{\rm p} = N_{\rm p\,lost}/N_{\rm p}$ is the relative number of test particles, precipitated during time interval Δt_i, τ_i and Δt_i are described above.

Dependencies of the normalized precipitating fluxes $\tilde{S} = S^{\rm num}_{\rm pr}/S^{\rm SD}_{\rm pr}$ on the time and energy are shown in Fig. 9. Precipitating fluxes $\tilde{S}_{\rm av}$, averaged over the whole

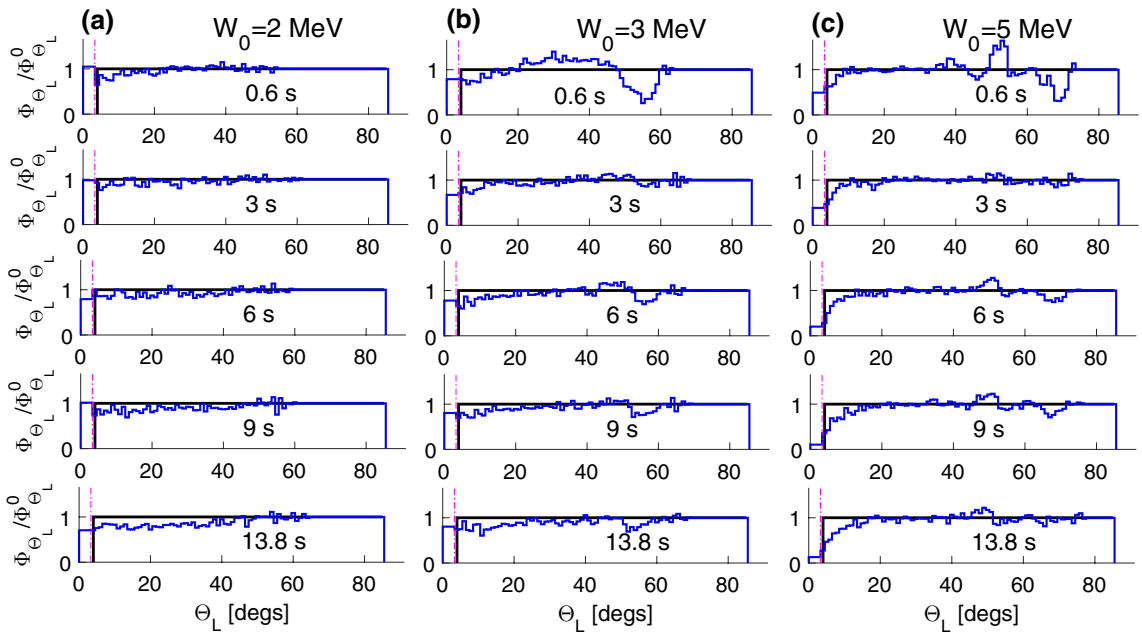

Fig. 8 Evolution of distribution function. Case II, time is counted from the beginning of simulation. Initial distribution is shown in black, the magenta line corresponds to the loss cone

simulation time, as well as maximum and minimum values, are shown in Fig. 10.

The energy dependence of time-averaged fluxes is similar for all three cases. At the lowest energy, $\tilde{S}_{\rm av} \approx 0.4$–$0.6$, then it increases to $\tilde{S}_{\rm av} \approx 1$ and is nearly constant for an interval about 1 MeV ($W_0 = 4$–5 MeV for Case I; $W_0 = 2$ –3 MeV for Case II; $W_0 = 4.5$–5.5 MeV for Case III) and then decreases, to values $\tilde{S}_{\rm av} \leq 0.25$ at the right boundary of the energy range.

The maximum values of precipitating fluxes correspond to the case of strong diffusion, i.e., to an almost isotropic distribution function in the vicinity of the loss cone (see Fig. 8). These cases correspond to the strongest interaction at $\Theta_L < 40°$, i.e., the most effective force bunching, the highest values of precipitating pitch angles Θ_{Lsc} and the widest range of Θ_{Lsc} (see Fig. 6b–d). In Case II, there is an energy range (2.5 MeV$\leq W_0 \leq$ 3.0 MeV), for which $S_{\rm pr}^{\rm num}/S_{\rm pr}^{\rm SD} \sim 1$ and trapping by the wave influences the precipitation (see Fig. 7c and 7d). In Cases I and III for energies corresponding to maximum fluxes trapping is not possible (see Fig. 4e and 4f).

The time dependence for maximum precipitating fluxes is not significant: fluxes oscillate near the average value. For lower and higher energies, when $S_{\rm pr}^{\rm num}/S_{\rm pr}^{\rm SD} < 1$, temporal dynamics of the fluxes is determined by generation of higher-frequency waves at the trailing edge, dissipation of the lower-frequency waves at the leading edge and propagation effects. For particles with lower energies, resonance points are located closer to the trailing edge (for rising tone packets, see (Grach and Demekhov 2018a, 2020a)), thus the resonant interaction is influenced by the generation of higher-frequency waves. When the generation takes place during the simulation, precipitating fluxes for lower energies increase with time (Cases I and III); when the generation is finished and wave packet propagates away from the equator, precipitating fluxes for lower energies decrease with time (Case II and model Gaussian packet in (Grach and Demekhov 2020a)). For particles with higher energies and low pitch angles (which determine the precipitation), resonant interaction, on the contrary, is influenced by the dissipation of lower-frequency waves at the leading edge. Thus, before the dissipation starts, precipitating fluxes for higher energies increase with time (Case I and model Gaussian packet in (Grach and Demekhov 2020a)) due to propagation effects; when the dissipation takes place precipitating fluxes for higher energies either fluctuate near an average value (Case III) or decrease with time (Case II).

It is also important to note that the temporal dynamics of the precipitating fluxes in the linear regime (higher energies) agrees with temporal dynamics of σ_μ (see Fig. 5 and relevant discussion) and thus with temporal dynamics of diffusion coefficients. The decrease of $\tilde{S}_{\rm av}$ with energy once the precipitation becomes linear is slowest for the case with lowest frequencies at the leading edge (Case III). Under similar wave amplitudes lower frequencies at the leading edge lead to smaller values of R for low pitch angles and higher energies, which in turn leads to larger σ_μ.

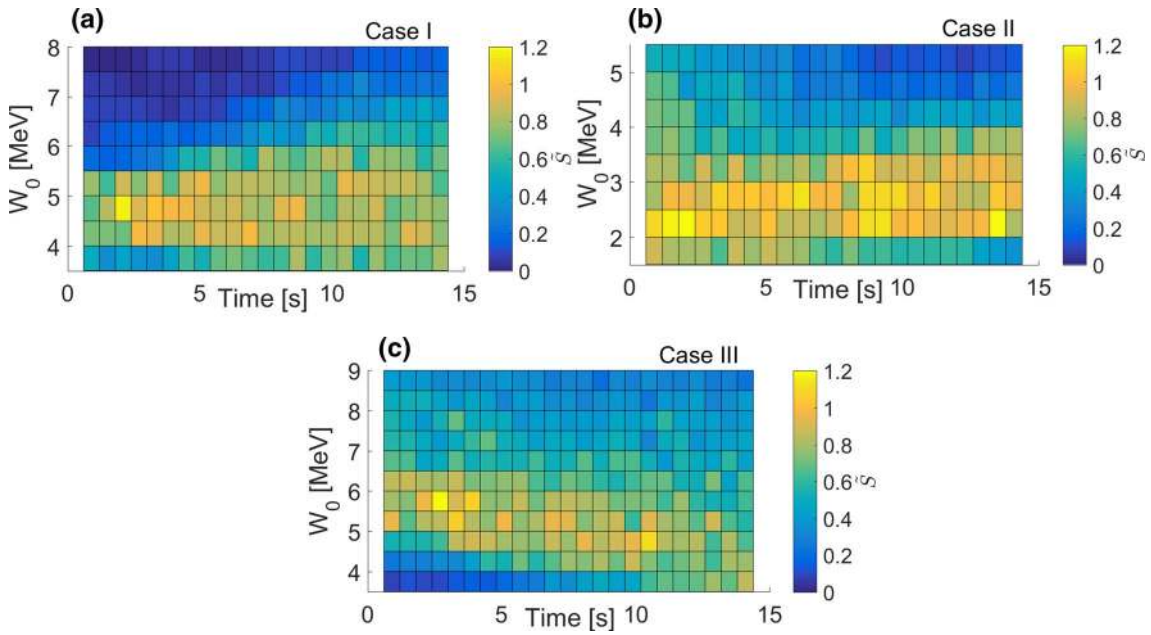

Fig. 9 Temporal dynamics of normalized precipitating fluxes for Case I (**a**), II (**b**) and III (**c**)

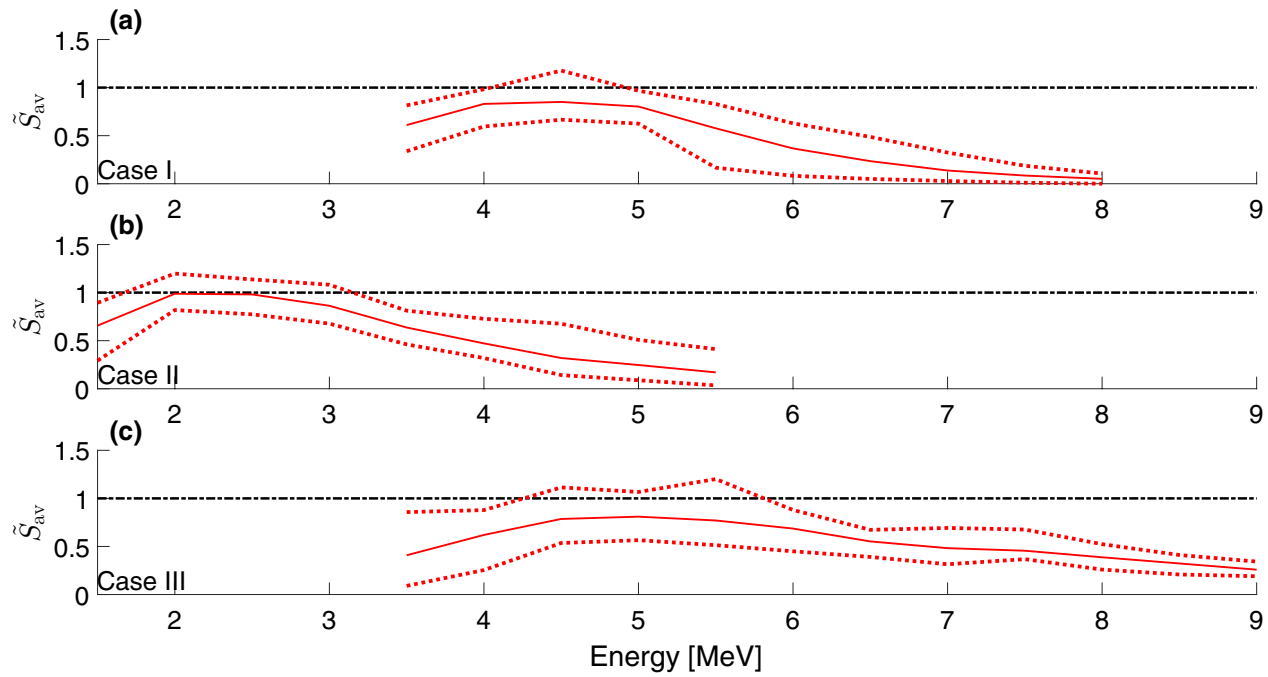

Fig. 10 Normalized precipitating fluxes, averaged (solid lines), maximized (dotted lines) and minimized (dotted lines) over the simulation time, for Case I (**a**), II (**b**) and III (**c**)

Note that Cases I and II actually belong to the same wave packet (element 14) with strong amplitude modulation and simulation for Case II starts 20 s after simulation for Case I ends (see Fig. 2). Thus, for element 14, we can assume a significant change in energy spectrum of precipitated particles on a time scale about 30 s. Within one simulation (15 s), there also can be a slight change of precipitated particles energy spectrum, caused by the wave packet evolution: the flux maximum on energy can become smoother (Case I), more pronounced (Case II) or shift to lower energies (Case III).

The temporal dynamics of precipitated fluxes and the energy spectrum of precipitating particles is generally in qualitative agreement with the results of (Kubota and Omura 2017), corresponding to the case when trapping does not cause direct precipitation (the case with low cold plasma density).

Summary

We have studied the resonant interaction of relativistic electrons with EMIC wave packets within one event (11:50–13:50 UT, 14 September 2017, Van Allen Probe B). The considered wave packets have rising tone within proton band and amplitudes up to 1.2 nT.

As a result of interaction with the wave packets under consideration, electrons with energies of 1.5–9 MeV can effectively precipitate into the loss cone. For particles with energies 2–5 MeV (depending on the wave packet and time interval), the precipitating flux is close to the limiting value corresponding to the strong diffusion regime.

The influence of a realistic wave packet structure brings the following specific features in the interaction, compared with idealized cases considered earlier (Grach and Demekhov 2020a).

For the considered short time intervals, the approximation of each local amplitude maximum of the wave packet by a Gaussian amplitude profile and a linear frequency drift gives a satisfactory description of the resonant interaction dynamics. At the same time, generation of higher-frequency waves at the packet trailing edge near the equator and dissipation of lower-frequency waves in the He^+ gyroresonance region at the leading edge can play an important role.

Generation of higher-frequency waves mostly influences interaction for electrons with lower energies and/or higher equatorial pitch angles, i.e. the particles, for which nonlinear interaction takes place. As long as the higher-frequency parts of the wave packet are generated near the equator with high enough amplitudes, the precipitating flux at lower energies increases. Once the generation stops and the wave propagates away from the equator, the corresponding precipitating flux decreases.

Dissipation of lower-frequency waves mostly affects interaction for particles with higher energies and low equatorial pitch angles, i.e., linear interaction. Once the dissipation starts, precipitating flux for particles with higher energies decreases with time. If there is no dissipation in the considered time interval, precipitating flux for higher energy particles (linear precipitation) will increase with time.

The amplitude modulation of the wave packet leads to a significant change of energy spectrum of precipitated particles during short time. Specifically, for element 14 of the considered event (three local amplitude maxima), the energy with maximum precipitating flux decreases from $W_0 \approx 4.5$ MeV to $W_0 \approx 2.5$ MeV during 30 s, while the element itself exists for about 120 s.

The main nonlinear effects, which affect the precipitation, are the force bunching and nonlinear shift of the resonance point. Force bunching blocks precipitation for particles with low pitch angles, up to $\Theta_L \approx 20°$. At the same time, the precipitation can exist from a noticeable range of higher $\Theta_L \approx 10°$–$30°$. This situation corresponds to maximum precipitating fluxes.

Particle trapping by the wave field can indirectly influence precipitation for some energies, but this influence is not crucial for the considered parameters. Effective precipitation due to trapping and directed scattering is possible for longer and higher-amplitude wave packets (amplitudes up to 14 nT are observed (Nakamura et al. 2019)) and also for higher cold plasma density (Kubota and Omura 2017; Grach and Demekhov 2018a, b).

In summary, for EMIC wave packets with amplitudes around 1 nT nonlinear effects play an important role in the formation of precipitating fluxes, even in the cases when wave packets are short and trapping by the wave field is not effective. Model wave packets with main parameters based on observations give a satisfactory description of precipitation dynamics, but real fine structure of a wave packet influences actual values of precipitating fluxes very significantly. It may be of interest to study other specific cases corresponding to real observations, and this will be a subject of future work.

Abbreviations
EMIC:: Electromagnetic ion-cyclotron; PSD:: Power spectral density.

Acknowledgements
The authors would like to thank the designers of Van Allen Probes and developers of the instruments (EMFISIS — Craig Kletzing) for the open access to the data.

Authors' contributions
VSG: numerical simulations, structure and strategy of the paper, and writing the paper. AGD: structure and strategy of the paper, model formulation and interpreting of the results, editing of the paper. AVL: processing of EMFISIS data and distinguishing of discrete elements from the dynamic spectrum. All authors read and approved the final manuscript.

Funding
The work of V.S. Grach (numerical simulations) in this study was supported by the Russian Science Foundation, grant No. 19–72–10111. The work of A.G. Demekhov (model formulation and interpreting of the results) was carried out as a part of State Assignment of Ministry of Education and Science of the Russian Federation, project No. 0030-2021-0002.

Availability of data and materials
Van Allen Probe data used in this paper can be found in the EMFISIS (https://emfisis.physics.uiowa.edu/data/index).

Declarations

Competing interests
The authors declare that they have no competing interests.

Author details
[1]Institute of Applied Physics of the Russian Academy of Sciences, Nizhny Novgorod, Russia. [2]Polar Geophysical Institute, Apatity, Russia.

Received: 25 March 2021 Accepted: 5 June 2021
Published online: 21 June 2021

References
Albert JM (1993) Cyclotron resonance in an inhomogeneous magnetic field. Phys Fluids B 5(8):2744–2750. https://doi.org/10.1063/1.860715

Albert JM (2000) Gyroresonant interactions of radiation belt particles with a monochromatic electromagnetic wave. J Geophys Res Space Phys 105(A9):21,191-21,209. https://doi.org/10.1029/2000JA000008

Albert JM, Bortnik J (2009) Nonlinear interaction of radiation belt electrons with electromagnetic ion cyclotron waves. Geophys Res Lett 36(12):L12110. https://doi.org/10.1029/2009GL038904

Albert JM, Tao X, Bortnik J (2012), Aspects of Nonlinear Wave-Particle Interactions. In: Summers D, Mann IR, Baker DN and Shulz M (ed) D. N. Baker, and M. Schulz Geophys. Monograph Series. vol 199. Dynamics of the Earth's Radiation Belts and Inner Magnetosphere, American Geophysical Union, Washington, D.C., pp. 255–264. https://doi.org/10.1029/2012gm001324

Artemyev AV, Mourenas D, Agapitov OV, Vainchtein DL, Mozer FS, Krasnoselskikh V (2015) Stability of relativistic electron trapping by strong whistler or electromagnetic ion cyclotron waves. Phys Plasmas 22(8):082901. https://doi.org/10.1063/1.4927774

Artemyev AV, Neishtadt AI, Vasiliev AA, Mourenas D (2017) Probabilistic approach to nonlinear wave-particle resonant interaction. Phys Rev E 95(2):023204. https://doi.org/10.1103/PhysRevE.95.023204

Bespalov PA, Trakhtengerts VY (1986) The cyclotron instability in the Earth radiation belts. In: Leontovich MA (ed) Rev Plasma Phys, vol 10. Plenum Publ, N.Y., pp 155–293

Chen L, Thorne RM, Bortnik J, Zhang XJ (2016) Nonresonant interactions of electromagnetic ion cyclotron waves with relativistic electrons. J Geophys Res Space Phys 121(10):9913–9925. https://doi.org/10.1002/2016JA022813

Demekhov A (2007) Recent progress in understanding Pc1 pearl formation. J Atmosph Solar-Terrestr Phys 69:1609–1622. https://doi.org/10.1016/j.jastp.2007.01.014

Demekhov AG, Trakhtengerts VY, Rycroft MJ, Nunn D (2006) Electron acceleration in the magnetosphere by whistler-mode waves of varying frequency. Geomagn Aeron 46:711–716. https://doi.org/10.1134/S0016793206060053

Demekhov AG, Trakhtengerts VY, Rycroft M, Nunn D (2009) Efficiency of electron acceleration in the Earth's magnetosphere by whistler mode waves. Geomagn Aeron 49(1):24–29. https://doi.org/10.1134/S0016793209010034

Engebretson MJ, Keiling A, Fornacon KH, Cattell CA, Johnson JR, Posch JL, Quick SR, Glassmeier KH, Parks GK, Rème H (2007) Cluster observations of Pc 1 2 waves and associated ion distributions during the October and November 2003 magnetic storms. Planet Space Sci 55:829–848. https://doi.org/10.1016/j.pss.2006.03.015

Engebretson MJ, Posch JL, Westerman AM, Otto NJ, Slavin JA, Le G, Strangeway RJ, Lessard MR (2008) Temporal and spatial characteristics of pc1 waves observed by st5. J Geophys Res Space Phys 113(A7):A07206. https://doi.org/10.1029/2008JA013145

Gan L, Li W, Ma Q, Albert JM, Artemyev AV, Bortnik J (2020) Nonlinear interactions between radiation belt electrons and chorus waves: Dependence on wave amplitude modulation. Geophys Res Lett 47(4):e2019GL085987. https://doi.org/10.1029/2019GL085987

Grach VS, Demekhov AG (2018a) Resonance interaction of relativistic electrons with ion-cyclotron waves. i. specific features of the nonlinear interaction regimes. Radiophys Quant Electr 60(12):942–959. https://doi.org/10.1007/s11141-018-9860-0

Grach VS, Demekhov AG (2018b) Resonant interaction of relativistic electrons with electromagnetic ion-cyclotron waves. II. Integral parameters of interaction regimes. Radiophys Quant Electr 61(6):389–401. https://doi.org/10.1007/s11141-018-9900-9

Grach VS, Demekhov AG (2020a) Precipitation of relativistic electrons under resonant interaction with electromagnetic ion cyclotron wave packets. J Geophys Res Space Phys 125(2):e2019JA027358. https://doi.org/10.1029/2019JA027358

Grach VS, Demekhov AG (2020b) Regimes of resonant interactions of electrons with auroral kilometric radiation. Radiophys Quant Electr 63(3):157–176. https://doi.org/10.1007/s11141-021-10043-5

Hiraga R, Omura Y (2020) Acceleration mechanism of radiation belt electrons through interaction with multi-subpacket chorus waves. Earth Planets Space 72(1):21. https://doi.org/10.1186/s40623-020-1134-3

Jordanova VK, Albert J, Miyoshi Y (2008) Relativistic electron precipitation by emic waves from self-consistent global simulations. J Geophys Res Space Phys 113(A3):A00A10. https://doi.org/10.1029/2008JA013239

Kangas J, Guglielmi A, Pokhotelov O (1998) Morphology and physics of short-period magnetic pulsations. Space Sci Rev 83:435–512

Karpman VI, Istomin YN, Shklyar DR (1974) Nonlinear theory of a quasimonochromatic whistler mode packet in inhomogeneous plasma. Plasma Phys 16(8):685–703. https://doi.org/10.1088/0032-1028/16/8/001

Kennel CF, Petschek HE (1966) Limit on stably trapped particle fluxes. J Geophys Res 71(1):1–28. https://doi.org/10.1029/JZ071i001p00001

Kitahara M, Katoh Y (2019) Anomalous trapping of low pitch angle electrons by coherent whistler mode waves. J Geophys Res Space Phys 124(7):5568–5583. https://doi.org/10.1029/2019JA026493

Kletzing CA, Kurth WS, Acuna M, MacDowall RJ, Torbert RB, Averkamp T, Bodet D, Bounds SR, Chutter M, Connerney J, Crawford D, Dolan JS, Dvorsky R, Hospodarsky GB, Howard J, Jordanova V, Johnson RA, Kirchner DL, Mokrzycki B, Needell G, Odom J, Mark D, Pfaff R, Phillips JR, Piker CW, Remington SL, Rowland D, Santolik O, Schnurr R, Sheppard D, Smith CW, Thorne RM, Tyler J (2013) The electric and magnetic field instrument suite and integrated science (EMFISIS) on RBSP. Space Sci Rev 179(1–4):127–181. https://doi.org/10.1007/s11214-013-9993-6

Krivolutsky AA, Repnev AI (2012) Impact of space energetic particles on the Earth's atmosphere (a review). Geomagn Aeron 52(6):685–716. https://doi.org/10.1134/S0016793212060060

Kubota Y, Omura Y (2017) Rapid precipitation of radiation belt electrons induced by emic rising tone emissions localized in longitude inside and outside the plasmapause. J Geophys Res Space Phys 122(1):293–309. https://doi.org/10.1002/2016JA023267

Larchenko AV, Demekhov AG, Kozelov BV (2019) The parameterization method of discrete VLF chorus emissions. Radiophy Quant Electr 62(3):159–173. https://doi.org/10.1007/s11141-019-09964-z

Li W, Hudson MK (2019) Earth's Van Allen Radiation Belts: From Discovery to the Van Allen Probes Era. J Geophys Res Space Phys 124(11):8319–8351. https://doi.org/10.1029/2018JA025940

Loto'Aniu TM, Fraser BJ, Waters CL (2005) Propagation of electromagnetic ion cyclotron wave energy in the magnetosphere. J Geophys Res Space Phys 110:A07214. https://doi.org/10.1029/2004JA010816

Lundin BV, Shkliar DR (1977) Interaction of electrons with low transverse velocities with VLF waves in an inhomogeneous plasma. Geomagnet Aeron 17:246–251

Lyons LR, Thorne RM (1973) Equilibrium structure of radiation belt electrons. J Geophys Res 78(13):2142–2149. https://doi.org/10.1029/JA078i013p02142

Mauk BH, Fox NJ, Kanekal SG, Kessel RL, Sibeck DG, Ukhorskiy A (2013) Science objectives and rationale for the radiation belt storm probes mission. Space Sci Rev 179(1–4):3–27. https://doi.org/10.1007/s11214-012-9908-y

Millan RM, Thorne R (2007) Review of radiation belt relativistic electron losses. J Atmosph Solar-Terrestr Phys 69(3):362–377. https://doi.org/10.1016/j.jastp.2006.06.019

Mironova IA, Aplin KL, Arnold F, Bazilevskaya GA, Harrison RG, Krivolutsky AA, Nicoll KA, Rozanov EV, Turunen E, Usoskin IG (2015) Energetic particle influence on the Earth's atmosphere. Space Sci Rev 194(1–4):1–96. https://doi.org/10.1007/s11214-015-0185-4

Morley SK, Friedel RHW, Cayton TE, Noveroske E (2010) A rapid, global and prolonged electron radiation belt dropout observed with the global positioning system constellation. Geophys Res Lett 37:6. https://doi.org/10.1029/2010GL042772

Nakamura S, Omura Y, Kletzing C, Baker DN (2019) Rapid precipitation of relativistic electron by EMIC rising-tone emissions observed by the van allen probes. J Geophys Res Space Phys 124(8):6701–6714. https://doi.org/10.1029/2019JA026772

Omura Y, Zhao Q (2012) Nonlinear pitch angle scattering of relativistic electrons by emic waves in the inner magnetosphere. J Geophys Res Space Phys 117(A8):A08227. https://doi.org/10.1029/2012JA017943

Omura Y, Zhao Q (2013) Relativistic electron microbursts due to nonlinear pitch angle scattering by emic triggered emissions. J Geophys Res Space Phys 118(8):5008–5020. https://doi.org/10.1002/jgra.50477

Pickett JS, Grison B, Omura Y, Engebretson MJ, Dandouras I, Masson A, Adrian ML, Santolík O, Décréau PME, Cornilleau-Wehrlin N, Constantinescu D (2010) Cluster observations of EMIC triggered emissions in association with Pc1 waves near Earth's plasmapause. Geophys Res Lett 37:L09104. https://doi.org/10.1029/2010GL042648

Shklyar D, Matsumoto H (2009) Oblique whistler-mode waves in the inhomogeneous magnetospheric plasma: resonant interactions with energetic charged particles. Surv Geophys 30(2):55–104. https://doi.org/10.1007/s10712-009-9061-7

Shprits YY, Chen L, Thorne RM (2009) Simulations of pitch angle scattering of relativistic electrons with mlt-dependent diffusion coefficients. J Geophys Res Space Phys 114(A3):A03,219. https://doi.org/10.1029/2008JA013695

Summers D, Thorne RM (2003) Relativistic electron pitch-angle scattering by electromagnetic ion cyclotron waves during geomagnetic storms. J Geophys Res Space Phys 108(A4):1143. https://doi.org/10.1029/2002JA009489

Suvorov EV, Tokman MD (1988) Generation of accelerated electrons during cyclotron heating of plasmas. Soviet J Plasma Phys 14(8):557–561

Tao X, Bortnik J, Thorne RM, Albert JM, Li W (2012) Effects of amplitude modulation on nonlinear interactions between electrons and chorus waves. Geophys Res Lett 39(6):L06102. https://doi.org/10.1029/2012GL051202

Thorne RM, Kennel CF (1971) Relativistic electron precipitation during magnetic storm main phase. J Geophys Res 76(19):4446–4453. https://doi.org/10.1029/JA076i019p04446

Trakhtengerts VY, Rycroft MJ (2000) Whistler-electron interactions in the magnetosphere: new results and novel approaches. J Atmosph Solar-Terrestr Phys 62(17–18):1719–1733. https://doi.org/10.1016/S1364-6826(00)00122-X

Trakhtengerts VY, Rycroft MJ (2008) Whistler and Alfvén mode cyclotron masers in space. Cambridge University Press, New York, Cambridge Atmospheric and Space Sciences Series

Tverskoy BA (1969) Main mechanisms in the formation of the Earth's radiation belts. Rev Geophys Space Phys 7:219–231. https://doi.org/10.1029/RG007i001p00219

Zhang XJ, Thorne R, Artemyev A, Mourenas D, Angelopoulos V, Bortnik J, Kletzing CA, Kurth WS, Hospodarsky GB (2018) Properties of intense field-aligned lower-band chorus waves: implications for nonlinear wave-particle interactions. J Geophys Res Space Phys 123(7):5379–5393. https://doi.org/10.1029/2018JA025390

Zhang XJ, Agapitov O, Artemyev AV, Mourenas D, Angelopoulos V, Kurth WS, Bonnell JW, Hospodarsky GB (2020) Phase decoherence within intense chorus wave packets constrains the efficiency of nonlinear resonant electron acceleration. Geophys Res Lett 47(20):e2020GL089807. https://doi.org/10.1029/2020GL089807

Publisher's Note